Ultrawideband Radar Cross-Section Reduction by a Metasurface Based on Defect Lattices and Multiwave Destructive Interference

Jianxun Su,[1,2] Huan He,[1] Yao Lu,[1] Hongcheng Yin,[1,2] Guanghong Liu,[3] and Zengrui Li[1,*]

[1]*School of Information Engineering, Communication University of China, Beijing 100024, China*

[2]*Science and Technology on Electromagnetic Scattering Laboratory, Beijing 100854, China*

[3]*Information Science Academy, China Electronics Technology Group Corporation (CETC), Beijing 100015, China*

A metasurface based on defect lattices and an alternative physical mechanism, multiwave destructive interference (MWDI), is proposed for ultrawideband radar cross-section (RCS) reduction. The bandwidth of RCS reduction (σ_R) is greatly expanded by second destructive interference. The metasurface is composed of 16 basic defect lattices. First, the defect lattice can generate primary destructive interference with the capacity of RCS reduction and amplitude-phase manipulation, which consists of an aperiodic array of square rings with an embedded cross. Second, the interference between multiple backscattered waves produced by the defect lattices at multiple frequencies sampled in an ultrawide band is simultaneously manipulated and optimized by the principle of superposition of waves and particle swarm optimization (PSO) to obtain second destructive interference. The metasurface enables a 10-dB RCS reduction over an ultrawide frequency band ranging from 6.16 to 41.63 GHz with a ratio bandwidth (f_H/f_L) of 6.76:1 under normal incidence for both polarizations. The estimated, simulated, and measured results are in good agreement and prove that the proposed metasurface is of great significance for bandwidth expansion of RCS reduction.

I. INTRODUCTION

In physics, interference is a phenomenon in which two or more waves of the same type superpose to form a resultant wave of greater, lower, or the same amplitude [1,2]. The interference usually refers to the interaction of waves that are correlated or coherent with each other. The principle of superposition of waves states that when two or more propagating waves traverse into the same space, the resultant amplitude is the vector sum of the amplitudes of the individual waves [3–5]. Interference effects can be observed with all types of waves, for example, light, radio, acoustic, surface water waves, or elastic waves.

Metasurfaces, which are essentially two-dimensional (2D) metamaterials with low fabrication cost, are capable of generating abrupt interfacial phase changes and providing a unique way of fully controlling the local wavefront at the subwavelength scale [6–9]. One of the potential applications of metasurfaces is to reduce the scattering field of a metal object. Generally, the RCS reduction can be achieved by two ways. One is electromagnetic (em) wave absorption, and the other is phase cancellation or destructive interference. For the absorptive method, the radar absorbing metamaterial can also be used for radar

cross-section (RCS) reduction by transforming electromagnetic energy into heat [10–13]. However, metamaterial absorbers usually operate in the vicinity of the resonance frequency. For the phase cancellation method, the scattered energy could be redirected away from the source direction.

As a traditional phase cancellation method, opposite phase cancellation has been widely implemented to achieve the RCS reduction. A 180° phase reversal is generated for two reflection coefficients, resulting in destructive interference.

Since the frequencies and directions of the incoming waves are unpredictable, in reality, bandwidth and oblique incidence performance are two important factors of stealth technology [14]. In 2007, Paquay *et al.* combined the perfect electric conductors (PEC) and artificial magnetic conductors (AMC) to design a checkerboard surface [15]. The backscattered field is successfully suppressed near the broadside direction of the surface. However, the RCS reduction occurs over a very narrow bandwidth owing to the limited in-phase reflection characteristics of the AMC. Then, a planar broadband checkerboard structure formed by combining two AMC cells is presented for wideband RCS reduction in Ref. [16]. The 41% fractional bandwidth (FBW) is obtained for 10-dB RCS reduction. In Ref. [17], a 2D phase gradient metasurface designed using a square combination of 49 split-ring subunit cells

---

*zrli@cuc.edu.cn

044088-1

is proposed to reduce RCS. In the frequency range of 7.8–17 GHz (74.19% FBW), RCS reduction is larger than 10 dB. In Ref. [18], an AMC structure is designed to achieve ultrawideband RCS reduction. This three-layer structure is composed of two trefoil-type AMC unit cells with different heights and relative permittivities in a chessboardlike configuration. The 10-dB bandwidth spans from 13.1 to 44.5 GHz (109% FBW). In Ref. [19], a planar low cost and thin metasurface is composed of two different AMC unit cells, which have Jerusalem cross patterns with different thicknesses. The metasurface reduces RCS more than 10 dB from 13.6 to 45.5 GHz (108% FBW) for both TE and TM polarizations. Different from previous metasurface designs that mainly focus on one dimension, a shared aperture metasurface design is divided into two dimensions [20]. Square patches are selected as metasurface elements to construct the metasurface, printed on both sides of the dielectric substrate. An air substrate is added between the dielectric substrate and the ground plane. This metasurface can achieve 10-dB RCS reduction almost from 4.8 to 17.5 GHz (113.9% FBW) under normal incidence. Furthermore, many other metasurfaces have been presented in previous research [21–23]. These checkerboard surfaces of periodic phase arrangement can create four strong scattering beams, which are bad for the bistatic RCS.

Recently, alternative designs of a coding diffuse metasurface, which can provide a more flexible way for the manipulation of reflected waves, have become highly desirable. In Ref. [24], coding, digital, and programmable metamaterials with excellent abilities for manipulating em waves were presented, and a 10-dB RCS reduction bandwidth of 66.67% was achieved. Then two metasurfaces using a windmill-shaped unit was developed. The metasurface in Ref. [25] realizes a 10-dB RCS reduction from 7 to 13 GHz, and the other shows a 10-dB RCS reduction within the whole *X* band [26]. A single-layer terahertz metasurface is proposed in Ref. [27], which produces untralow reflections from 1 to 1.8 THz. Based on a three-layer polarization convertor, an ultrabroadband reflective metamaterial is presented in Ref. [28]. The bandwidth of 10-dB RCS reduction covers from 5.21 to 15.09 GHz (94.38% FBW) under normal incidence. In Ref. [29], a broadband and wide-angle 2-bit coding metasurface is designed and characterized at terahertz (THz) frequencies. The ultrathin metasurface is composed of four digital elements based on a metallic double-cross line structure, resulting in 60% FBW for 10-dB RCS reduction. In Ref. [30], a metasurface composed of three kinds of simply patterned elements with different resonant properties is designed. The metasurface shows excellent backward scattering from 0.77 to 1.97 THz. A broadband and broadangle polarization-independent random coding metasurface is investigated in Ref. [31]. The metasurface attains a 10-dB RCS reduction bandwidth of 84.75%. In Ref. [32],

two kinds of AMC unit cells constitute a coding diffuse metasurface, which realizes a 10-dB RCS reduction from 5.4 to 7.4 GHz. Then, a coding phase gradient metasurface constructed by phase gradient metasurfaces as the coding elements was proposed in Ref. [33]. A 10-dB RCS reduction bandwidth of 64.18% was realized. In Ref. [34], a random combinational gradient metasurface was proposed for broadband, wide-angle, and polarization-independent diffusion scattering. The metasurface suppresses the RCS by more than 10 dB within the frequency band from 7.1 to 15.6 GHz (74.89% FBW). Compared to the checkerboard metasurfaces with periodic phase arrangement, the reflection energy is distributed into more directions away from the source direction by the coding diffuse metasurfaces, which results in a lower bistatic RCS.

The objective of this work is to develop a defect lattice structure and an alternative physical mechanism of multiwave destructive interference (MWDI) for breaking the bandwidth constraints of traditional phase cancellation methods such as opposite phase cancellation. The defect lattices, which destroy the periodicity of the finite array, are capable of generating amplitude-phase manipulated waves. The defect lattices themselves can achieve primary destructive interference, leading to RCS reduction. The interference between the local backscattered waves generated by the defect lattices is simultaneously manipulated and optimized by the superposition principle of waves and particle swarm optimization (PSO) to obtain second destructive interference. The proposed metasurface can achieve a 10-dB RCS reduction from 6.16 to 41.63 GHz with a ratio bandwidth (RBW) of 6.76:1 under normal incidence. A comparison between other recent research and this work is provided in Table I. Obviously, our results are far beyond the state of the art of the performance in terms of bandwidth of this type of structure.

TABLE I. Comparison of our work and previous research.

Article	σ_R (dB)	OFB (GHz)	FBW (%)	RBW (f_H/f_L)
[16]	10	14.5–21.8	41	1.50:1
[17]	10	7.8–17	74.19	2.18:1
[24]	10	7.5–15	66.67	2.00:1
[28]	10	5.21–15.09	94.38	2.90:1
[29]	10	700–1300	60	1.86:1
[21]	10	3.8–10.7	95	2.82:1
[22]	10	6.1–17.8	98	2.92:1
[31]	10	17–42	84.75	2.47:1
[33]	10	9.83–19.12	64.18	1.95:1
[23]	10	5.4–14.2	89.8	2.63:1
[18]	10	13.1–44.5	109	3.40:1
[19]	10	13.6–45.5	108	3.35:1
[20]	10	4.8–17.5	113.9	3.65:1
This Work	10	6.16–41.63	148.4	6.76:1

OFB: The operating frequency band.

This paper is organized as follows. Section II shows the alternative physical mechanism of MWDI. The design process of an ultrawideband RCS reducer metasurface is shown in Sec. III. The simulated results for normal and oblique incidences are illustrated in Sec. IV, and the measured monostatic RCS reduction under normal incidence is shown in Sec. V. The conclusions are drawn in Sec. VI.

II. MULTIWAVE DESTRUCTIVE INTERFERENCE

A metasurface consists of a 2D array of $M \times N$ defect lattices. Figure 1 shows the design flowchart for the RCS reducer metasurface. First, the lattice structure is designed to produce amplitude-phase manipulated waves and overcome the short circuit problem in an ultrawide frequency band. Second, the combination of the alternative mechanism of MWDI and PSO algorithm is adopted to optimize and determine the geometric parameters of the defect lattices for achieving ultrawideband monostatic RCS reduction. Third, the defect lattices are arranged randomly to make up the metasurface. Fourth, em simulation is carried out by the transient solver of CST Microwave Studio® to verify the performance of monostatic and bistatic RCS reductions. Finally, the high-precision RCS

measurement is conducted to validate the theoretical design and simulation.

The main theory for the metasurface design is the defect lattice and the combination of MWDI and PSO algorithm. The $M \times N$ defect lattices are uniformly spaced with d_x in the x direction and d_y in the y direction, as shown in Fig. 2. The defect structures, which destroy the periodicity of the finite array, are capable of generating a reverse current, leading to primary destructive interference. $M \times N$ backscattered waves (yellow arrows) with full control of amplitude and phase produced locally by the defect lattices are superimposed and optimized to achieve second destructive interference, as shown in Fig. 3.

The RCS reduction (σ_R) of the metasurface for second destructive interference compared to an equal-sized PEC surface can be represented by [35]

$$\sigma_R = 10 \log_{10} \left[\frac{|E_{MS}^s|^2}{|E_{PEC}^s|^2} \right] = 20 \log_{10} \left| \frac{\sum\limits_{m=1}^{M} \sum\limits_{n=1}^{N} |E_{m,n}^s| e^{j \angle E_{m,n}^s}}{MN |E_{m,n}^i| e^{j \angle E_{m,n}^i}} \right|,$$
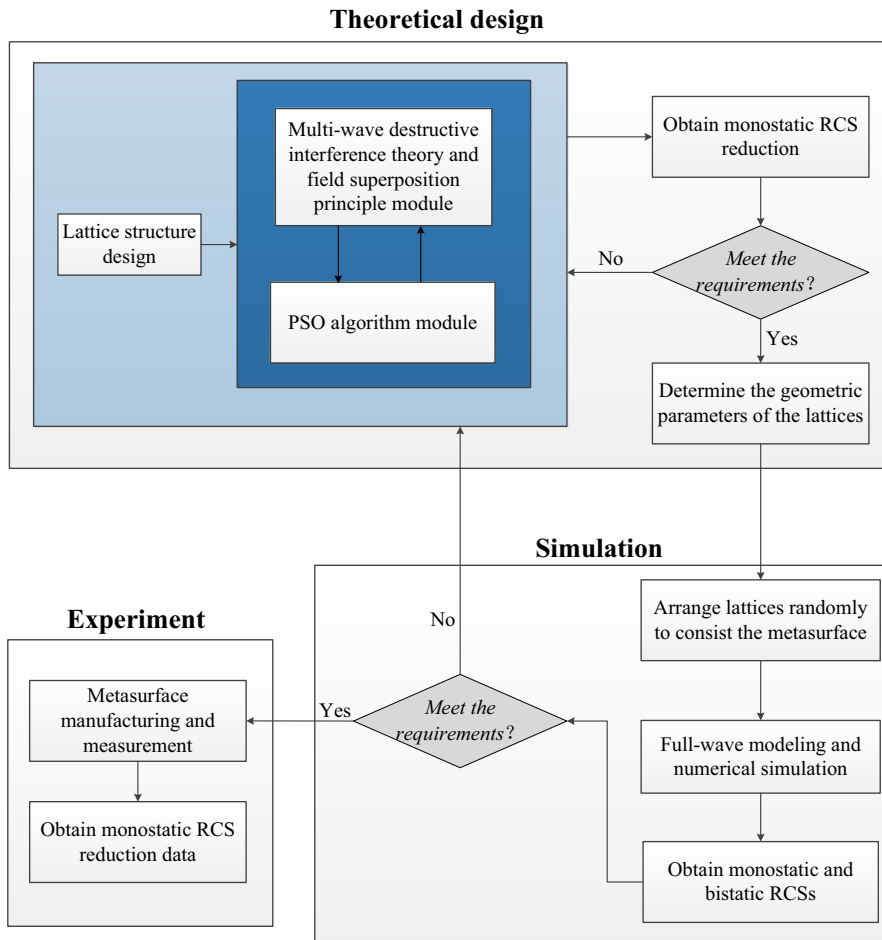
(1)

FIG. 1. The design procedure of the metasurface.

Theoretical design
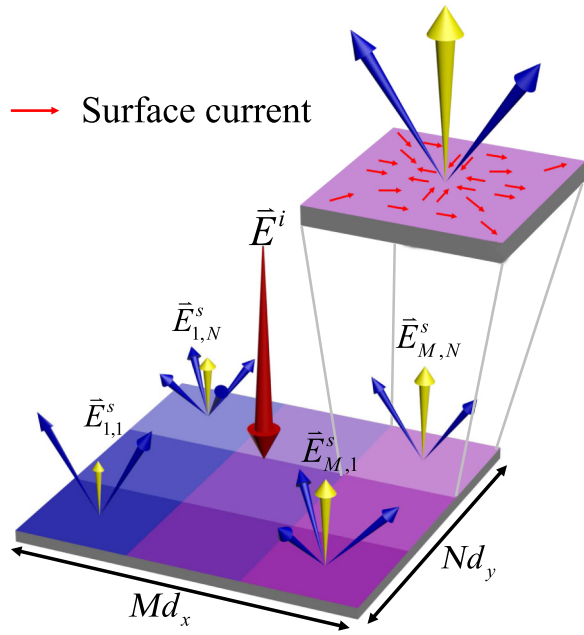
Experiment

Simulation

FIG. 2. Plane wave is illuminating on a metasurface consisting of $M \times N$ defect lattices. $M \times N$ amplitude-phase manipulated waves are produced locally by the defect lattices. The yellow arrows indicate backscattered waves while the blue arrows represent side-scattered waves or side lobes.

where E_{MS}^s and E_{PEC}^s are the scattering fields of the metasurface and equal-sized PEC surface, respectively. $E_{m,n}^s$ and $E_{m,n}^i$ are the scattering field and incident field of the (m, n)th lattice, respectively. Based on the measurement method of a frequency selective surface, the reflection coefficient of the (m, n)th defect lattice is defined as
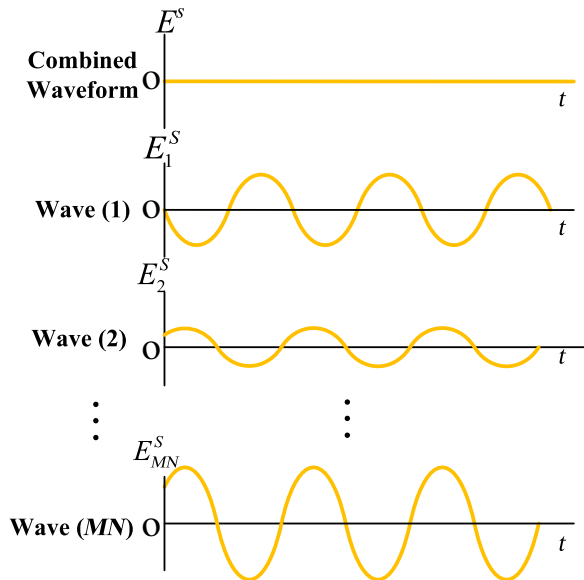
$$\Gamma_{m,n} = |\Gamma_{m,n}|e^{j \angle \Gamma_{m,n}} = \frac{|E_{m,n}^s|}{|E_{m,n}^i|}e^{j \angle E_{m,n}^s}. \qquad (2)$$

Thus, the total RCS reduction can be approximated by

$$\sigma_R = 20 \log_{10} \frac{\left| \sum_{m=1}^{M} \sum_{n=1}^{N} |\Gamma_{m,n}|e^{j \angle \Gamma_{m,n}} \right|}{MN}. \qquad (3)$$

Eliminating the phase term in Eq. (3), the RCS reduction for primary destructive interference just produced by the defect lattices themselves is described as

$$\sigma_R^{1\mathrm{st}} = 20 \log_{10} \frac{\sum_{m=1}^{M} \sum_{n=1}^{N} |\Gamma_{m,n}|}{MN}. \qquad (4)$$

Complete destructive interference requires

$$\sum_{m=1}^{M} \sum_{n=1}^{N} |E_{m,n}^s|e^{j \angle E_{m,n}^s} = 0, \qquad (5)$$

which is an indefinite equation. The amplitude and phase of $M \times N$ backscattered waves can be manipulated independently and optimized to achieve ultrawideband destructive interference. It is noted that Eq. (5) has countless solutions. Obviously, opposite phase cancellation and coding metamaterials are just two special solutions. If there are two electric fields, complete destructive interference requires two electric fields with equal amplitude and opposite phase, as shown in Fig. 4. If the number of electric fields is greater than two, there will be countless cases for achieving complete destructive interference. These cases shown in Fig. 5, which are the solutions of the above indefinite equation, can also achieve complete phase cancellation. The phase difference between the electric fields is variable. However, opposite phase cancellation and coding metamaterials would exclude these cases. For opposite phase cancellation and coding metamaterials, due to the fixed number of unit cells and the fixed phase difference between them, the ability to realize phase cancellation is greatly reduced, leading to a narrow bandwidth of RCS reduction.

Here, a metasurface based on defect lattices and a physical mechanism of MWDI is proposed for ultrawideband RCS reduction. Due to the presence of a reverse current, the defect lattices can generate amplitude- and

FIG. 3. The combined waveform of $M \times N$ backscattered waves with full control of the reflection amplitude and phase.

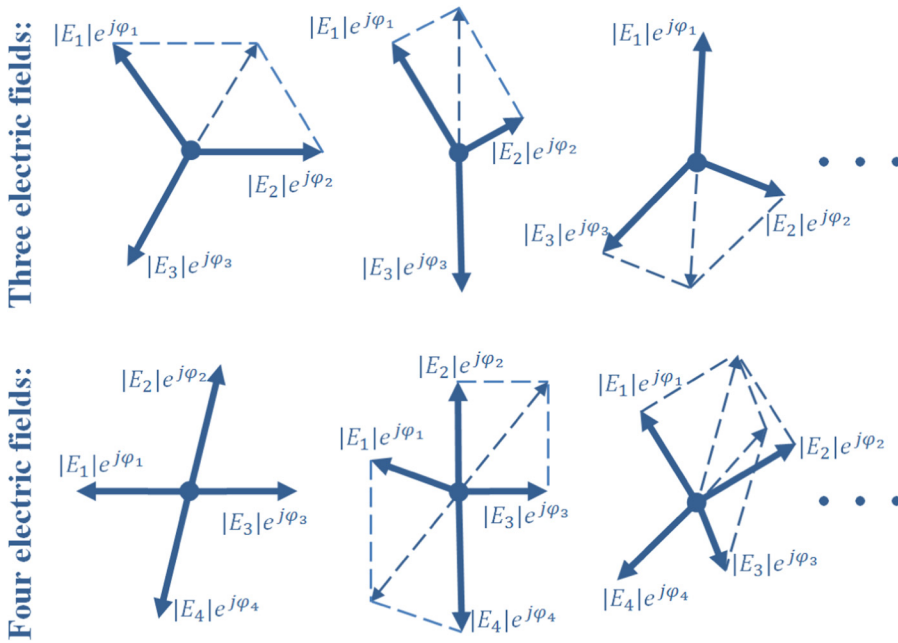FIG. 4. Opposite phase cancellation of two electric fields.

FIG. 5.   Complete destructive interference for three and four electric fields.

phase-manipulated waves and has the capacity of primary destructive interference and RCS reduction. As depicted in Fig. 3, multiple backscattered waves from the defect lattices are superimposed and optimized to achieve second destructive interference. More defect lattices and, in particular, full control of both the amplitude and phase of the reflection between them greatly increase the ability to control em waves and achieve the maximum bandwidth of RCS reduction.

III. METASURFACE DESIGN

The design process of ultrawideband RCS reducer metasurface is shown in this section.

A. Defect lattice and its reflection characteristics

The basic lattice used in this work is a defect structure with variable layer thickness, which is different from the traditional lattice of a single-layer finite array. The single-layer structure of a traditional lattice suffers from a serious short-circuit problem, resulting in a narrow bandwidth. In addition, the traditional lattice with uniform current distribution just has the capacity of phase manipulation, whose reflection amplitude is approximately equal to unity. Based on the traditional lattice consisting of a finite array with 7×7 square-ring patches, nine square-ring patches in the middle part are replaced by a cross patch to constitute the proposed defect lattice. The geometry structure of the defect lattice is depicted in Fig. 6. The metallic patches are printed on the surface of a polytetrafluoroethylene woven glass (Model: F4B-2, Wangling Insulating Materials, Taizhou, China) substrate with a dielectric constant $\varepsilon_r = 2.65$, and loss tangent $\tan \delta = 0.001$. The layer

thickness h is variable. The back of the substrate is the metallic ground plane. The side length of the square ring is L. The length and width of the cross strips are $5L$ and L, respectively.

The alternative defect lattice has several advances. First, the defect structures, which destroy the periodicity of the finite array, are capable of generating amplitude- and phase-manipulated waves. Second, variable layer thickness can overcome the short circuit problem of the single-layer structure, leading to a narrow bandwidth. Third, a wave path difference is produced between lattices
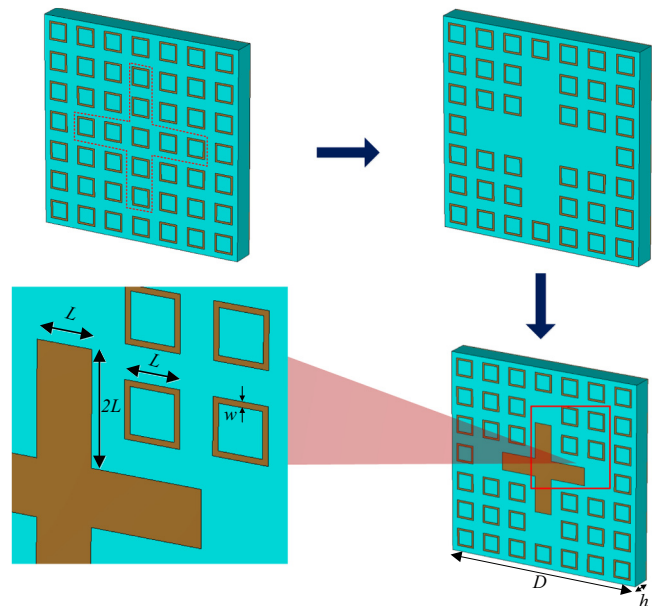

FIG. 6.   Geometrical structure of the defect lattice. Dimensions are: $a = 8$, $w = 0.3$, $h = 2, 4, 6$ in mm.
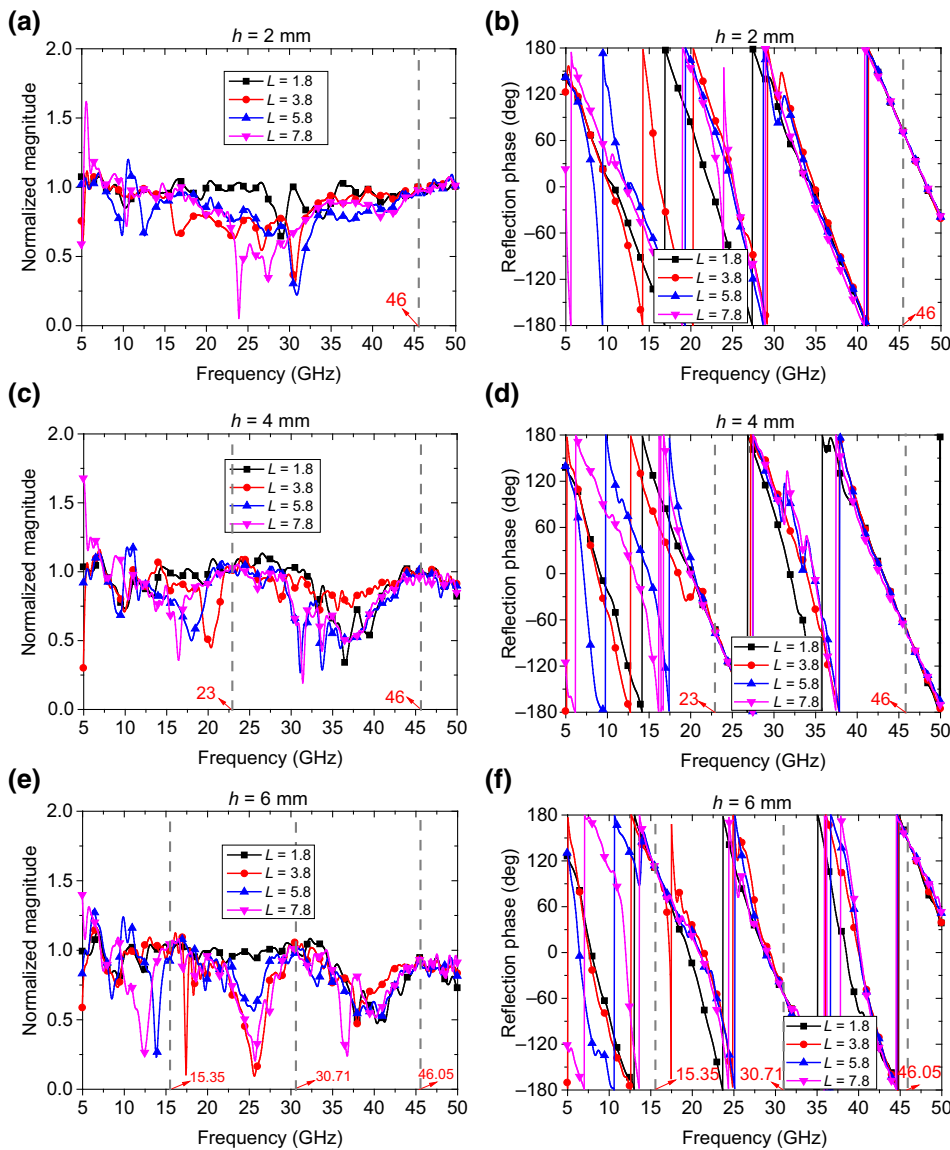
FIG. 7. The reflection coefficients of the basic defect lattices. (a, c, e) The normalized amplitudes and (b, d, f) the reflection phases with the change of geometer parameter L for the layer thicknesses of 2, 4, and 6 mm, respectively.

with different thicknesses. This additional phase difference can extend the coverage range of the reflected phase over an ultrawide frequency band. The range of the reflection phase changes is large enough with the change of geometrical parameter L, and the reflection amplitude can be less than unity. This means the defect lattice itself has the capacity of RCS reduction and amplitude manipulation. This amplitude and phase feature guarantee the possibility of superwideband manipulation of em waves and the realization of second destructive interference. The innovation of the defect lattice is illustrated below by simulation.

The lattices are simulated by the transient solver of CST Microwave Studio®. In this simulation, the periodicity a of the unit cell and the width w of a square ring are fixed. Therefore, two geometrical parameters are controlled to tailor em wave reflection characteristics. The geometrical parameter L varies from 0.8 to 7.8 mm with a step size of 0.1 mm, while there are three choices of

layer thicknesses for the dielectric substrate: 2, 4, and 6 mm. A part of the reflection amplitude and phase curves are plotted in Fig. 7. The lattice of the single-layer structure will limit the bandwidth for RCS reduction because of the short circuit problem at some frequencies. For the thickness $h = 6$ mm, the reflection phase around 15.35 and 30.71 GHz hardly depends on the value of L due to a short circuit. Transmission line theory can better explain this condition. The equivalent circuit model is shown in Fig. 8. The infinite metal ground is equivalent to the short circuit terminal. When the layer thickness $h = n\lambda_g/2$ ($n = 1, 2, 3 \ldots$), the patch is short circuited by the metal ground. $\lambda_g \left(= \lambda_0/\sqrt{\varepsilon_r}\right)$ is the waveguide wavelength. The layer thicknesses ($h = 6$ mm) are equal to $0.5\lambda_g$ and $1.0\lambda_g$ at 15.35 and 30.71 GHz, respectively. Therefore, the reflection phases at these two frequencies do not change with the size L of the patch, as shown in Fig. 7(f). In-phase superposition does not have the ability to reduce the RCS.
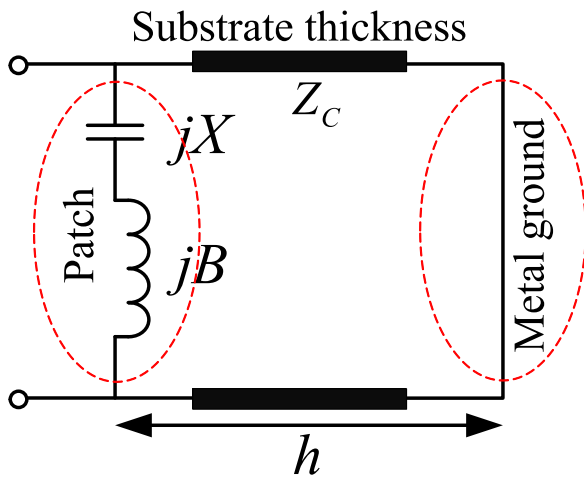
FIG. 8.   Equivalent circuit model.

However, other layer thicknesses ($h \neq 6$ mm) have a variable phase difference with the layer thickness $h = 6$ mm at 15.35 and 30.71 GHz when the patch size L changes. Thus, defect lattices with various layer thicknesses can effectively overcome the short circuit problems.

A comparison of the current distribution and the scattering pattern between the defect lattice and a traditional lattice is presented in Fig. 9. Due to the presence of a reverse current, the defect lattice produces primary destructive interference with several scattered beams, leading to RCS reduction and reflection amplitude manipulation. Full and free control of both the amplitude and phase of the local

waves would greatly increase the ability of ultrawideband manipulation of em waves and achieve second destructive interference.

B. Optimization design of the basic defect lattices

This is the most important step for achieving ultrawideband RCS reduction. The metasurface presented in this research is composed of 4×4 defect lattices. The backscattering field is only related to the reflection coefficient of the basic lattices, but is independent of their distribution under normal incidence. Thus, a combination of PSO and MWDI is utilized to optimize the geometrical parameters of 16 defect lattices for achieving the maximum bandwidth of the RCS reduction.

The PSO [36] is a new class of stochastic optimizers based on the collective behavior of nature, which is very easy to understand, easy to implement, and highly robust. It is similar in some ways to genetic algorithms, but requires less computational bookkeeping. It has been applied in conjunction with Eq. (3) to optimize the geometrical parameter L and layer thickness h of 16 defect lattices. The detailed flowchart for the PSO algorithm with MWDI module to optimize the design of the basic defect lattices is depicted in Fig. 10. The geometrical parameters ($L_{1,1}, \ldots L_{1,4}, \ldots L_{4,4}$) and ($h_{1,1}, \ldots h_{1,4}, \ldots h_{4,4}$) of 16 defect lattices are put into the MWDI module. The parameters L are initialized to be in the range of [0.8, 7.8] mm, while the thickness h is a discrete value chosen from the set {2, 4, 6} mm. The iteration number ($N_{\max}$) is set to 500 in the optimization.
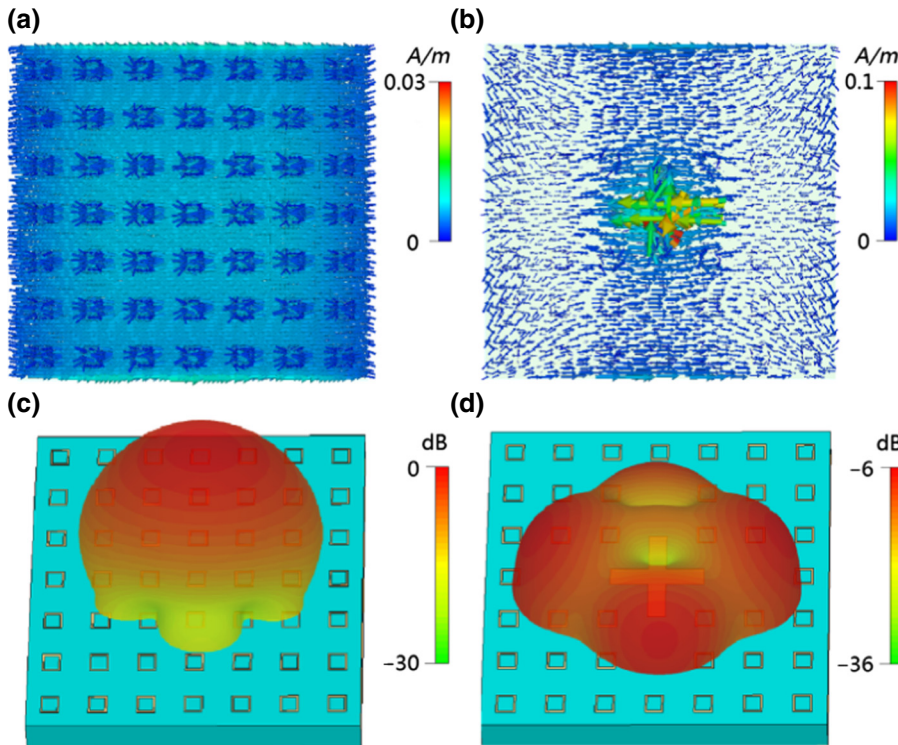

FIG. 9.   Comparison of the current distribution and scattering pattern of a lattice with $h = 6$ mm and $L = 3.1$ mm at 5.4 GHz. (a), (c) Traditional lattice. (b), (d) Defect lattice.
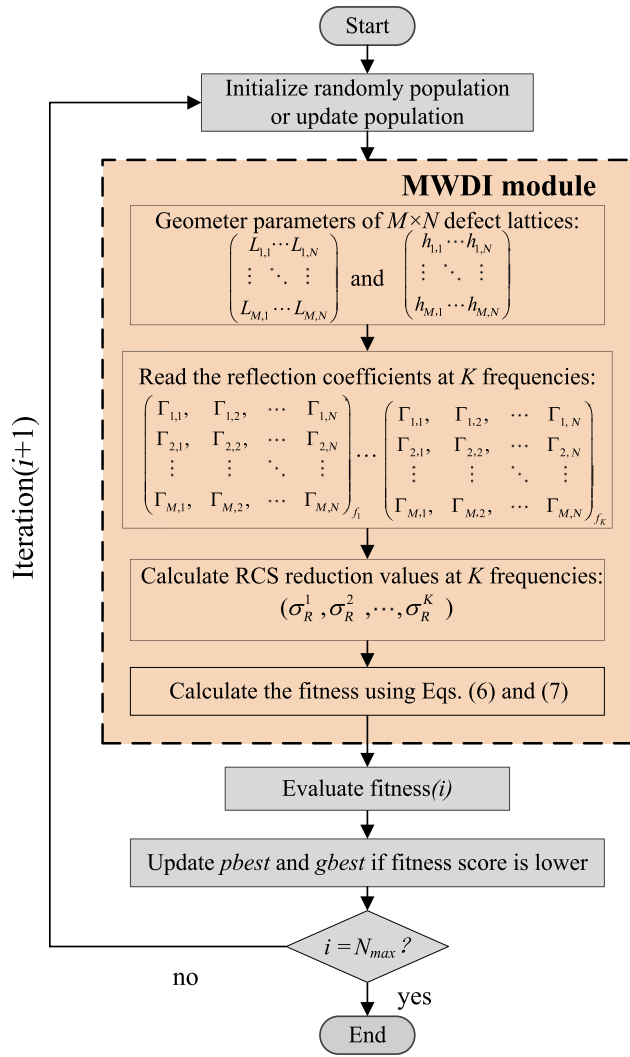
FIG. 10.   Optimization flowchart of the basic defect lattices for ultrawideband RCS reduction.

In the MWDI module, the reflection coefficients at K frequencies can be read from the precalculated reflection amplitude and phase table. Based on Eq. (3), the RCS reduction (σ_R) can be calculated. Taking into consideration that a cancellation error occurs when some frequencies have a very large σ_R value and others with a very small σ_R value, the fitness function used to assess the wideband RCS reduction performance is defined as

$$\text{fitness} = \sum_{i=1}^{K} s(i), \qquad (6)$$

and

$$s(i) = \begin{cases} 0, & \text{if } |\sigma_R^i + 12| \leq 1 \text{ dB} \\ 0.5, & \text{if } 1 \text{ dB} \leq |\sigma_R^i + 12| \leq 2 \text{ dB} \,, \\ 1.0, & \text{if } |\sigma_R^i + 12| > 2 \text{ dB} \end{cases} \qquad (7)$$

TABLE II.   Optimal results of geometrical parameter L and layer thickness h.

Lattice	1	2	3	4	5	6	7	8
L (mm)	1.4	6.9	6.5	1.5	7.4	6.3	7.0	2.4
h (mm)	6	2	6	6	6	4	6	2
Lattice	9	10	11	12	13	14	15	16
L (mm)	6.2	2.0	6.7	3.1	3.7	2.2	7.3	7.2
h (mm)	2	4	2	6	2	6	2	2

where σ_R^i is the backward RCS reduction under normal incidence at ith frequency. The optimized target value for RCS reduction is set to 12 dB. The redundancy of 2 dB is considered for the approximation error by Eq. (3) due to the coupling between the lattices and their edge effects. To get a better RCS reduction performance, the fitness should be as low as possible. Then the RCS reduction values are scored by Eq. (6). The output fitness score will be evaluated at each iteration. The individual optimal location (p_{best}) and the global optimal location (g_{best}) will be updated if the fitness score is lower. After 500 iterations, the optimal parameters ($L_{1,1}, \ldots L_{1,4}, \ldots L_{4,4}$) and ($h_{1,1}, \ldots h_{1,4}, \ldots h_{4,4}$) are obtained, which are listed in Table II. The proposed metasurface can be constituted by the optimized 16 defect lattices with the optimal parameters shown in Table II. Figure 11 gives the predicted monostatic RCS reduction of the metasurface with a plane wave normally impinging. RCS reduction values of more than 10 dB can be realized from 6.16 to 41.63 GHz, which is about 148.4% FBW and 6.76:1 RBW.

The estimated results indicate that the metasurface based on defect lattices and MWDI can greatly expand the bandwidth of the RCS reduction. The reflection amplitudes and phases of 16 defect lattices are shown in Figs. 12(a) and 12(b), respectively. The reflection amplitudes and phases are functions of frequency, but they can always
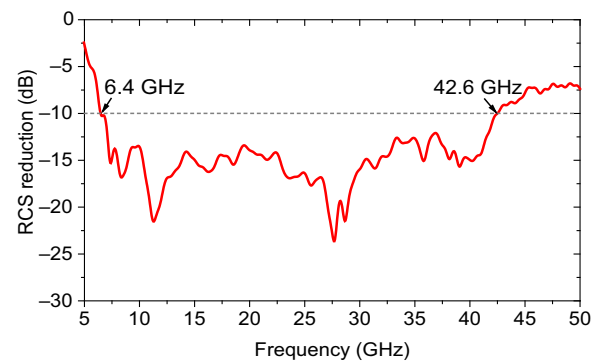

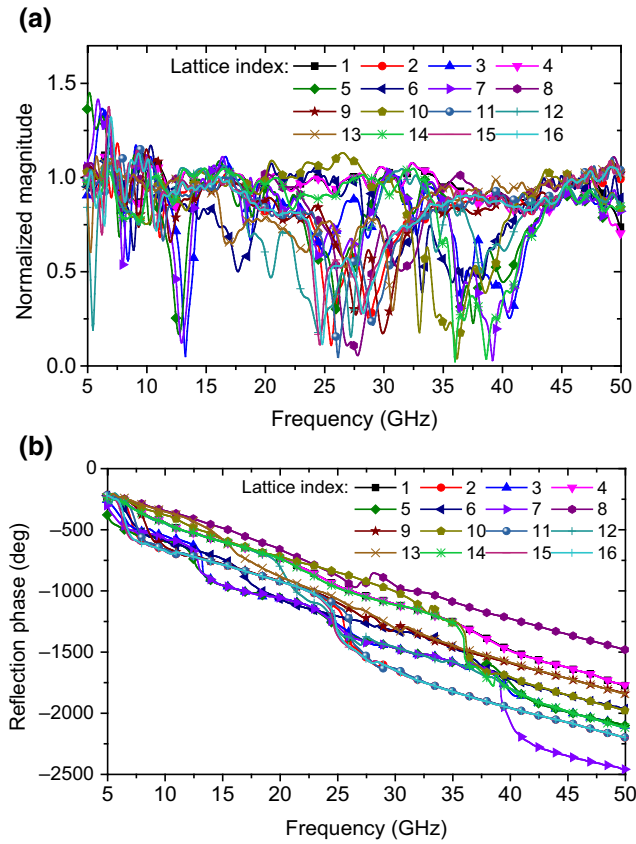FIG. 11.   The predicted monostatic RCS reduction under normal incidence.

(a)

(b)

FIG. 12. The reflection amplitudes and phases of 16 basic defect lattices.

FIG. 13. The RCS reduction produced by the defect lattices themselves.

satisfy

$$\left| \sum_{m=1}^{M} \sum_{n=1}^{N} \Gamma_{m,n} \right| \leq MN\sqrt{0.1}. \qquad (8)$$

The RCS reduction produced by defect lattices themselves is shown in Fig. 13. The presented MWDI together with the PSO algorithm are used to simultaneously control and optimize the amplitudes and phases of 16 defect lattices in an ultrawide frequency band to achieve good destructive interference.

IV. ULTRAWIDEBAND RCS REDUCTION PERFORMANCE

The metasurface is composed of these 16 basic defect lattices. The scattering pattern $E^s(\theta, \varphi)$ in space is determined by the arrangement of the basic defect lattices, except for the backward direction ($\theta = 0, \varphi = 0$). The diffusion scattering of em waves is caused by randomized lattice distribution, leading to a low bistatic RCS [37]. To facilitate manufacturing of the metasurface, the lattices with equal layer thicknesses are put together. The random distribution of 16 basic defect lattices and the full structure of the metasurface are depicted in Fig. 14. The model of the
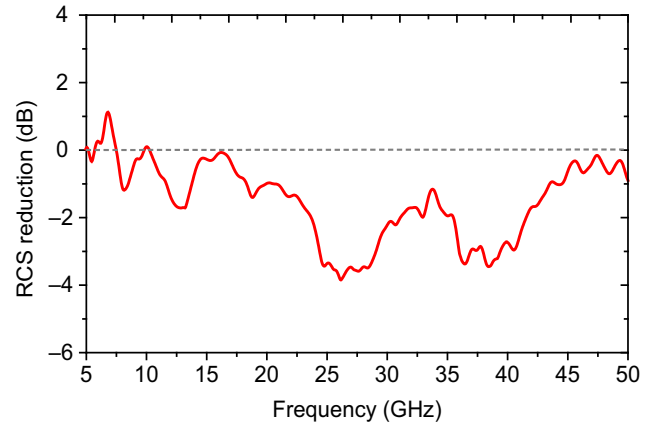
optimized RCS reducer metasurface is occupied by 4×4 defect lattices with overall dimensions of $224 \times 224 \text{ mm}^2$.

To investigate the RCS reduction of the proposed metasurface, the monostatic RCS of the metasurface as well as that of an equal-sized PEC surface are simulated by the transient solver of CST Microwave Studio® under normal incidence. The RCS reduction of the metasurface normalized to the equal-sized PEC surface under normal incidence is shown in Fig. 15. Almost the same results achieved for both polarizations exhibit the polarization-independent feature of the metasurface. Significant RCS reduction can be observed in the frequency band from 5 to 50 GHz. It can be seen that a 10-dB RCS reduction
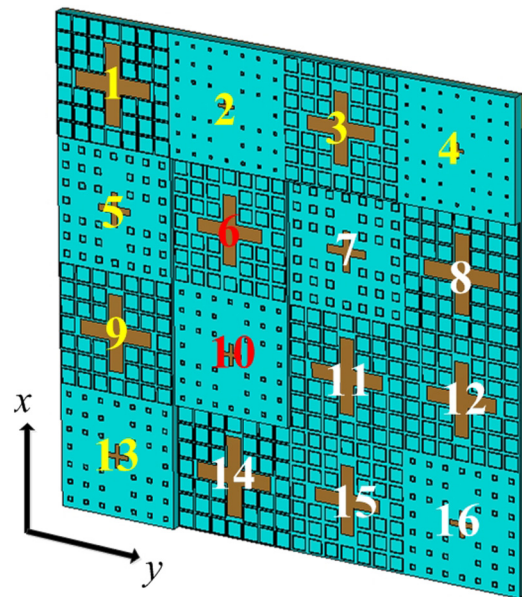

FIG. 14. The full CST model of the ultrawideband RCS reducer metasurface. The inserted index is the lattice number shown in Table II.
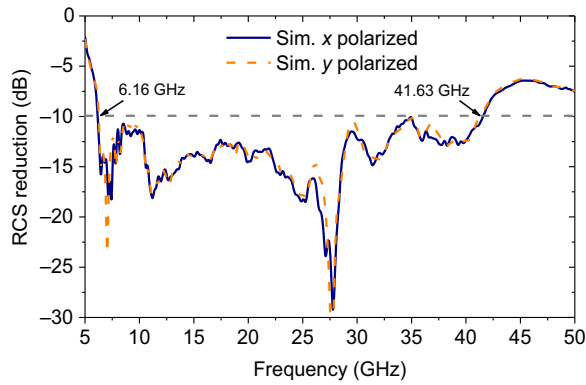
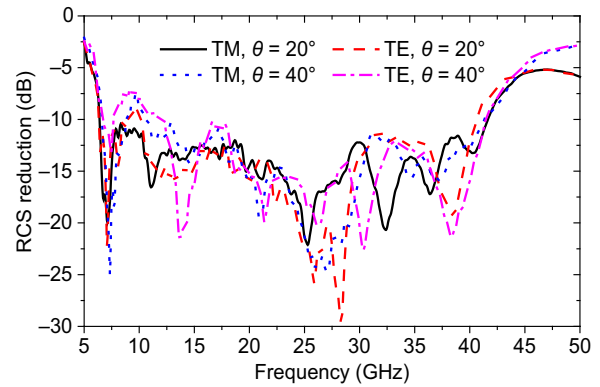FIG. 15. The simulated monostatic RCS reduction under normal incidence.

FIG. 17. The RCS reductions under wide-angle oblique incidences for both TE and TM polarizations. TE/TM: The direction of the electric or magnetic field is perpendicular to the plane of incidence.

is achieved in an ultrawide frequency band from 6.16 to 41.63 GHz with a RBW of 6.76:1. The proposed defect lattice and MWDI are shown to greatly expand the bandwidth of the RCS reduction. The simulation results are in good agreement with the estimated results, so the RCS reduction can be approximated by Eq. (3), which does not include edge effects, but provides a good guideline for RCS reduction of the metasurface compared to an equal-sized PEC surface.

Taking a further step, the three-dimensional (3D) bistatic RCS patterns of the designed metasurface and the equal-sized PEC surface under normal incidence are depicted in Fig. 16 at 7, 12, and 20 GHz, respectively. It can be observed that the bistatic RCS is dramatically decreased compared to the equal-sized PEC surface. The designed metasurface is capable of generating abrupt interfacial amplitude and phase changes. Due to the nonuniform distributions of the reflection amplitudes and phases of 16 defect lattices, the scattered fields are redirected to

other directions and the specular reflection is effectively suppressed.

For the case of oblique incidence, the simulated RCS reduction of the metasurface for TE and TM polarized waves as a function of frequency at different incident angles is shown in Fig. 17. The results indicate that a remarkable RCS reduction is achieved across the ultrawide frequency band (5–50 GHz) for both polarizations. Thus, for wide-angle incidences, the proposed metasurface still performs well in the operating frequency band.

V. EXPERIMENTAL VERIFICATION

To validate the effectiveness of the proposed RCS reduction structure, a sample manufactured using printed circuit board technology is measured to investigate the performance of the proposed metasurface. A 224×224 mm^2 square sample is shown in Fig. 18. Three pieces of
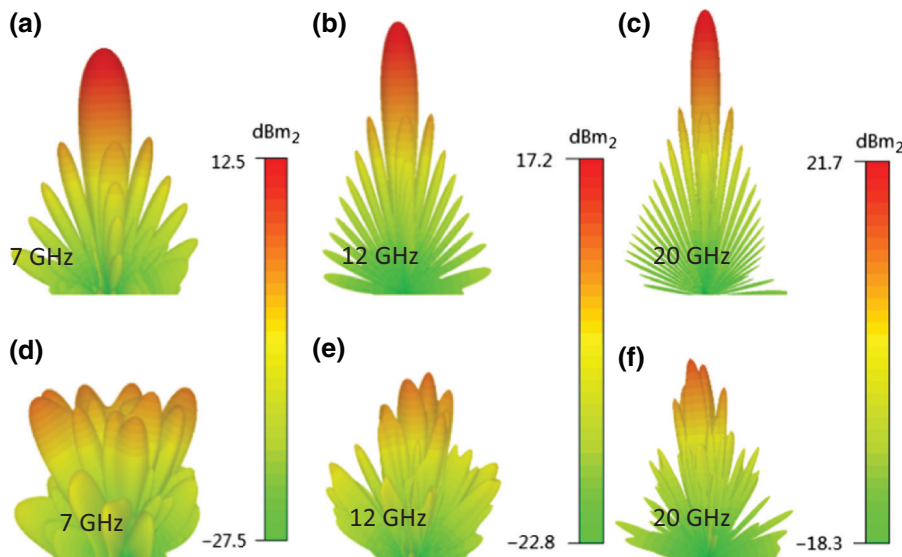

FIG. 16. Comparison of bistatic scattering patterns between the proposed metasurface and equal-sized PEC surface under *x* polarized wave normal incidence at 7, 12, and 20 GHz, respectively. (a)–(c) Specular reflection by the PEC surface. (d)–(f) Diffusion scattering by metasurface.
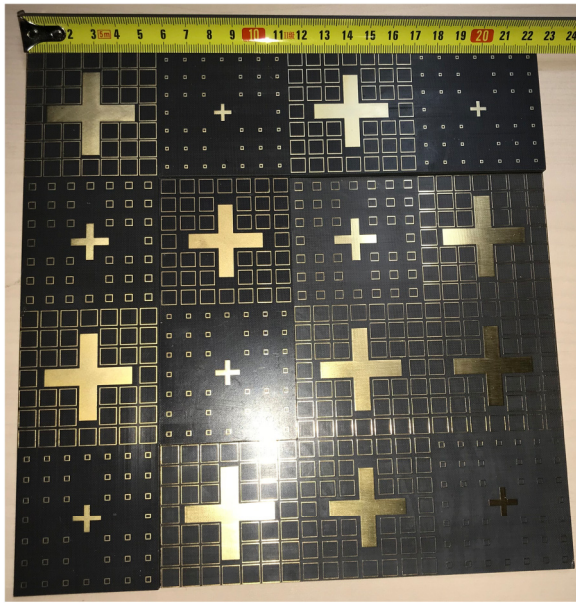
FIG. 18.   The photograph of the fabricated metasurface.

the metasurface board with different thicknesses are processed separately and then stitched together according to our metasurface design. The top and bottom copper layers with a thickness of 0.035 mm each are printed on a polytetrafluoroethylene woven glass substrate with a dielectric constant $\varepsilon_r = 2.65$ (loss tangent $\tan \delta = 0.001$). A high-precision RCS measurement is conducted using the compact antenna test range system of the Science and Technology on Electromagnetic Scattering Laboratory in Beijing, China, as depicted in Fig. 19. The spherical waves emitted by the horn antenna are reflected by the parabolic metal reflector and become a plane wave. The shortest distance between the metasurface sample and the reflector makes it easy to meet the far-field conditions.
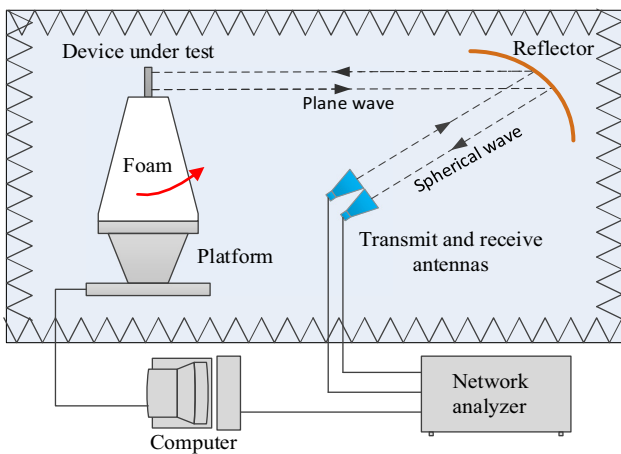

FIG. 19.   The schematic of compact antenna test range system for the monostatic RCS measurement.
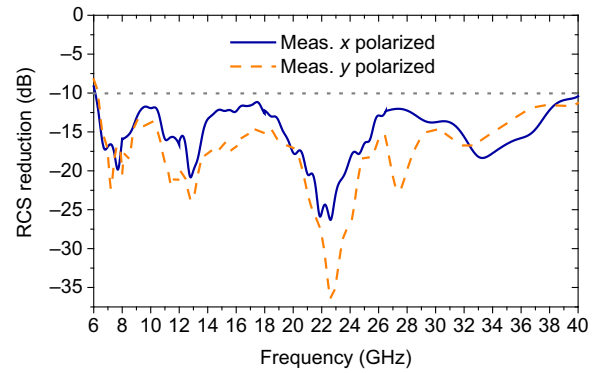

FIG. 20.   Measured RCS reduction for both polarizations under normal incidence.

Two horn antennas placed adjacently serve as a transmitter and a receiver, respectively. Due to the limitations of our equipment, the measurement could not be conducted in the frequency range higher than 40 GHz. The entire measured band from 6 to 40 GHz is covered by five pairs of standard linearly polarized horn antennas, which work at 6–8, 8–12, 12–18, 18–26.5, and 26.5–40 GHz, respectively. The antennas are connected to a vector network analyzer, which has the function of a time domain gating. The RCS of the metasurface and equal-sized copper ground of the metasurface are separately measured first. Then, subtraction is done to obtain the RCS reduction.

Figure 20 shows the measured monostatic RCS reduction of the sample under normal incidence. The RCS reduction maxima is more than 25 dB at 22.7 GHz, while the RCS of the sample is reduced by more than 10 dB within the frequency band of 6.28–40 GHz for both x and y polarized incident waves. The measured and the simulated RCS reduction results have excellent agreements over the entire frequency band. The value deviations can be attributed to manufacturing and measurement errors. Second destructive interference is achieved in an ultrawide frequency band. Overall, the ultrawideband RCS reduction and diffusion scattering by the proposed metasurface based on defect lattices and MWDI are confirmed.

VI. CONCLUSIONS

In this paper, an alternative metasurface, based on defect lattices and the alternative physical mechanism of MWDI, is investigated for greatly expanding the bandwidth of RCS reduction. The proposed metasurface can effectively obtain an ultrawideband, wide-angle, polarization-independent monostatic and bistatic RCS reduction. Sixteen defect lattices are employed to construct the metasurface, each of which is composed of an aperiodic array of square rings with an embedded cross with the capacity of RCS reduction and amplitude-phase manipulation. The primary destructive interference can be realized by the defect lattice

themselves. More basic lattices and full and free control of both the amplitude and phase of the reflection greatly improve the destructive interference performance. Interference between multiple local backscattered waves produced by the basic defect lattices at multiple frequencies sampled in an ultrawide frequency band is simultaneously manipulated and optimized by the superposition principle of waves and PSO to obtain second destructive interference. The simulated results demonstrate that the monostatic RCS reduction value exceeds 10 dB almost the entire band from 6.16 to 41.63 GHz compared with the RCS of the equal-sized PEC surface, with a ratio bandwidth of 6.76:1 for both polarizations under normal incidence. Moreover, the random lattice distribution has realized the diffusion scattering of em waves, which simultaneously contributes to a low bistatic RCS. The estimated, simulated, and measured results match quite well and validate that the proposed metasurface is significant for bandwidth expansion of RCS reduction.

[1] R. Becker, *Electromagnetic Field and Interactions* (Dover Publications, New York, NY, USA, 1982).

[2] H. J. Pain and P. Rankin, *Introduction to Vibrations and Waves* (Wiley, New York, NY, USA, 2015), 1st ed.

[3] A. H. Nurfaizey, J. Stanger, N. Tucker, N. Buunk, A. Wallace, M. P. Staiger, and J. Mater, Manipulation of electrospun fibres in flight: the principle of superposition of electric fields as a control method, J. Mater. Sci. **47**, 1156 (2012).

[4] J. Y. Li, Y. X. Qi, and S. G. Zhou, Shaped beam synthesis based on superposition principle and Taylor method, IEEE Trans. Antennas Propag. **65**, 11 (2017).

[5] G. H. Koopmann, L. M. Song, and J. B. Fahnline, A method for computing acoustic fields based on the principle of wave superposition, J. Acoust. Soc. Am. **86**, 3 (1989).

[6] J. B. Pendry, D. Schurig, and D. R. Smith, Controlling electromagnetic fields, Science **312**, 5781 (2006).

[7] L. Zhang, S. Mei, K. Huang, and C. W. Qiu, Advances in full control of electromagnetic waves with metasurfaces, Adv. Opt. Mater. **4**, 6 (2016).

[8] R. Liu, C. Ji, J. J. Mock, J. Y. Chin, T. J. Cui, and D. R. Smith, Broadband ground-plane cloak, Science **323**, 5912 (2009).

[9] X. H. Wang, F. Chen, and E. Semouchkina, Implementation of low scattering microwave cloaking by all-dielectric metamaterials, IEEE Microw. Wireless Compon. Lett. **23**, 2 (2013).

[10] D. Micheli, R. Pastore, C. Apollo, M. Marchetti, G. Gradoni, V. M. Primiani, and F. Moglie, Broadband electromagnetic absorbers using carbon nanostructure-based composites, IEEE Trans. Microw. Theory Tech. **59**, 10 (2011).

[11] C. M. Watts, X. Liu, and W. J. Padilla, Metamaterial electromagnetic wave absorbers, Adv. Mater. **24**, 23 (2012).

[12] M. Yoo, H. K. Kim, and S. Lim, Angular- and polarization-insensitive metamaterial absorber using subwavelength unit cell in multilayer technology, IEEE Antennas Wireless Propag. Lett. **15**, 414 (2016).

[13] H. B. Baskey and M. J. Akhtar, Design of flexible hybrid nano-composite structure based on frequency selective surface for wideband radar cross section reduction, IEEE Trans. Microw. Theory Tech. **65**, 6 (2017).

[14] O. I. Sukharevsky, *Electromagnetic Wave Scattering by Aerial and Ground Radar Objects* (CRC Press, Boca Raton, FL, USA, 2014), 1st ed.

[15] M. Paquay, J. C. Iriarte, I. Ederra, R. Gonzalo, and P. de Maagt, Thin AMC structure for radar cross-section reduction, IEEE Trans. Antennas Propag. **55**, 12 (2007).

[16] J. C. Iriarte Galarregui, A. T. Pereda, J. L. Matínez de Falcón, I. Ederra, R. Gonzalo, and P. D. Maagt, Broadband radar cross-section reduction using AMC technology, IEEE Trans. Antennas Propag. **61**, 12 (2013).

[17] Y. F. Li, J. Q. Zhang, S. B. Qu, J. F. Wang, H. Y. Chen, Z. Xu, and A. X. Zhang, Wideband radar cross section reduction using two-dimensional phase gradient metasurfaces, Appl. Phys. Lett. **104**, 221110 (2014).

[18] E. Ameri, S. H. Esmaeli, and S. H. Sedighy, Ultra wide band radar cross section reduction using multilayer artificial magnetic conductor metasurface, J. Phys. D: Appl. Phys. **51**, 285304 (2018).

[19] E. Ameri, S. H. Esmaeli, and S. H. Sedighy, Low cost and thin metasurface for ultra wide band and wide angle polarization insensitive radar cross section reduction, Appl. Phys. Lett. **112**, 201601 (2018).

[20] Y. J. Zheng, X. Y. Cao, J. Gao, H. H. Yang, Y. L. Zhou, and S. M. Wang, Shared aperture metasurface with ultra-wideband and wide-angle low-scattering performance, Opt. Mater. Express **7**, 2706 (2017).

[21] M. J. Haji-Ahmadi, V. Nayyeri, M. Soleimani, and O. M. Ramahi, Pixelated checkerboard metasurface for ultra-wideband radar cross section reduction, Sci. Rep. **7**, 11437 (2017).

[22] Y. T. Jia, Y. Liu, Y. J. Guo, K. Li, and S. X. Gong, A dual-patch polarization rotation reflective surface and its application to ultra-wideband RCS reduction, IEEE Trans. Antennas Propag. **65**, 3291 (2017).

[23] J. J. Xue, W. Jiang, and S. X. Gong, Chessboard AMC surface based on Quasi-Fractal structure for wideband RCS reduction, IEEE Antennas Wireless Propag. Lett. **17**, 2 (2018).

[24] T. J. Cui, M. Q. Qi, X. Wan, J. Zhao, and Q. Cheng, Coding metamaterials, digital metamaterials and programmable metamaterials, Light Sci. Appl. **3**, e218 (2014).

[25] K. Wang, J. Zhao, Q. Cheng, D. S. Dong, and T. J. Cui, Broadband and broad-angle low-scattering metasurface based on hybrid optimization algorithm, Sci. Rep. **4**, 5935 (2014).

[26] J. Chen, Q. Cheng, J. Zhao, D. S. Dong, and T. J. Cui, Reduction of radar cross section based on a metasurface, Prog. Electromagn. Res. **146**, 71 (2014).

[27] D. S. Dong, J. Yang, Q. Cheng, J. Zhao, L. H. Gao, S. J. Ma, S. Liu, H. B. Chen, Q. He, W. W. Liu, Z. Fang, L. Zhou, and T. J. Cui, Terahertz broadband low-reflection metasurface by controlling phase distributions, Adv. Opt. Mater. **3,** 10 (2015).

[28] S. J. Li, X. Y. Cao, L. M. Xu, L. J. Zhou, H. H. Yang, J. F. Han, Z. Zhang, D. Zhang, X. Liu, C. Zhang, Y. J. Zheng, and Y. Zhao, Ultra-broadband reflective metamaterial with RCS reduction based on polarization convertor, information entropy theory and genetic optimization algorithm, Sci. Rep. **6,** 37409 (2016).

[29] L. J. Liang, M. G. Wei, X. Yan, D. Q. Wei, D. C. Liang, J. G. Han, X. Ding, G. Y. Zhang, and J. Q. Yao, Broadband and wide-angle RCS reduction using a 2-bit coding ultrathin metasurface at terahertz frequencies, Sci. Rep. **6,** 39252 (2016).

[30] J. Zhao, Q. Cheng, T. Q. Wang, W. Yuan, and T. J. Cui, Fast design of broadband terahertz diffusion metasurfaces, Opt. Express **25,** 2 (2017).

[31] H. Y. Sun, C. Q. Gu, X. L. Chen, Z. Li, L. L. Liu, B. Z. Xu, and Z. C. Zhou, Broadband and broad-angle polarization-independent metasurface for radar cross section reduction, Sci. Rep. **7,** 40782 (2017).

[32] X. Liu, J. Gao, L. M. Xu, X. Y. Cao, Y. Zhao, and S. J. Li, A coding diffuse metasurface for RCS reduction, IEEE Antennas Wireless Propag. Lett. **16,** 724 (2017).

[33] Q. Q. Zheng, Y. F. Li, J. Q. Zhang, H. Ma, J. F. Wang, Y. Q. Pang, Y. J. Han, S. Sui, Y. Shen, H. Y. Chen, and S. B. Qu, Wideband, wide-angle coding phase gradient metasurfaces based on Pancharatnam-Berry phase, Sci. Rep. **7,** 43543 (2017).

[34] Y. Q. Zhuang, G. M. Wang, J. G. Liang, T. Cai, X. L. Tang, T. F. Guo, and Q. F. Zhang, Random combinatorial gradient metasurface for broadband, wide-angle and polarization-independent diffusion scattering, Sci. Rep. **7,** 16560 (2017).

[35] W. G. Chen, C. A. Balanis, and C. R. Birtcher, Checkerboard EBG surfaces for wideband radar cross section reduction, IEEE Trans. Antennas Propag. **63,** 6 (2015).

[36] D. W. Boeringer and D. H. Werner, Particle swarm optimization versus genetic algorithms for phased array synthesis, IEEE Trans. Antennas Propag. **52,** 3 (2004).

[37] L. H. Gao, Q. Cheng, J. Yang, S. J. Ma, J. Zhao, S. Liu, H. B. Chen, Q. He, W. X. Jiang, H. F. Ma, Q. Y. Wen, L. J. Liang, B. B. Jin, W. W. Liu, L. Zhou, J. Q. Yao, P. H. Wu, and T. J. Cui, Broadband diffusion of terahertz waves by multi-bit coding metasurfaces, Light Sci. Appl. **4,** e324 (2015).